Energy Reports 12 (2024) 4279–4293

Contents lists available at ScienceDirect

Energy Reports

journal homepage: www.elsevier.com/locate/egyr

Research Paper

Assessing the accuracy of analytical methods for extracting parameters of different PV module technologies under clear and cloudy sky conditions

M.A. Sevillano-Bendezú [a], V. Pleshcheva [b,c], B. Calsi [a], L.A. Conde [a], J. Montes-Romero [d], J. Aguilera [e], J. de la Casa [e], J.A. Töfflinger [a,*]

[a] Departamento Académico de Ciencias, Sección Física, Pontificia Universidad Católica del Perú, Av. Universitaria 1801, Lima 15088, Peru
[b] Departamento Académico de Ingeniería, Sección de Ingeniería Informática, Pontificia Universidad Católica del Perú, Av. Universitaria 1801, Lima 15088, Peru
[c] European School of Management and Technology, Schlossplatz 1, Berlin 10178, Germany
[d] Advances in Photovoltaic Technology, CEACTEMA, University of Jaén, Campus Las Lagunillas, Jaén 23071, Spain
[e] IDEA Research Group. Centre for Advanced Studies in Energy and Environment. University of Jaén, Campus Las Lagunillas, Jaén 23071, Spain

ARTICLE INFO

Keywords:
Photovoltaic modules
Single-diode model
Analytical extraction methods
Electrical parameters
Outdoor *I-V* curves

ABSTRACT

Accurately determining single-diode model parameters yields essential insights into the photovoltaic (PV) device performance and behavior. Analytical methods for extracting these parameters often rely on mathematical assumptions typically valid under controlled indoor conditions. Applying these methods to PV modules in the field introduces complexities due to varying environmental conditions and module technologies, leading to divergencies between parameters extracted under outdoor and indoor conditions. This study closes the gap in analyzing the retrieved parameters under intricate outdoor conditions by differentiating between all-, clear-, and cloudy-sky conditions and varying irradiances for different PV technologies. We examine three methods over a year of outdoor I-V curves from Al-BSF, HIT, and a-Si/μc-Si PV modules in Lima, Peru, a low-latitude site. The findings represent the first mid-term study by the country's premier laboratory uniquely equipped for diverse outdoor PV module characterization. We evaluate the accuracy of each method using the Normalized Root Mean Square Error (NRMSE) by comparing experimental against simulated I-V curves derived from the extracted parameters. Our findings reveal that the parameters for the Al-BSF and HIT modules under all-sky conditions align with reported outdoor trends for varying irradiances, while under clear skies, they correspond with indoor trends. In terms of accuracy, the methods by Phang et al. and de Blas et al. consistently achieve an average NRMSE below 1 % across all PV module types under all-sky conditions. However, when differentiating between sky conditions, the NRMSE values for the Al-BSF and HIT modules are notably lower under clear sky conditions at any irradiance level, preserving a mean value below 0.6 %, unlike the a-Si/μc-Si PV technology, which shows more consistent NRMSE values across all sky conditions and most irradiance levels and in average above 0.7 %. These results demonstrate that selecting sky conditions based on the evaluated PV technology is beneficial for enhanced accuracy in outdoor parameter extraction.

1. Introduction

Accurate electrical modeling of a solar photovoltaic (PV) generator is vital for predicting energy yield, optimizing design before implementation, monitoring the PV system, and identifying possible causes of losses and degradation (Humada et al., 2020; Baig et al., 2020; Farias-Basulto et al., 2023; Solís-Alemán et al., 2019; Caballero et al., 2018; Nofuentes and Almonacid, 1998; Deutsche Gesellschaft für, 2013). PV generator prediction, design, and monitoring can potentially affect PV project stakeholders' decision-making and financing strategies (Chin et al., 2015). Different models have been proposed for these purposes, some of them based on experimental *I-V* curves, which can express the performance indicators precisely (Karmalkar and Haneefa, 2008; Ulbrich et al., 2015; Nofuentes et al., 2013). Generally, these models are based on equivalent-circuit configurations, which simplify the microscopic nature of charge generation to an electric current source. Additionally, due to its rectifying property, the PV generator tends to be represented by a diode. It contains parasitic resistances such

* Corresponding author.
E-mail address: japalominot@pucp.edu.pe (J.A. Töfflinger).

https://doi.org/10.1016/j.egyr.2024.10.002
Received 29 May 2024; Received in revised form 18 August 2024; Accepted 1 October 2024
Available online 14 October 2024

as the series and shunt resistances in a more realistic representation. This last description corresponds to the single-diode (SD) model, which has a general character and can describe any PV generator, such as cells, modules, and arrays, assuming uniform conditions (Oulcaid et al., 2020; Premkumar et al., 2020) even applied on multi-junctions as presented by Nouri et al. (2024). Other models were also proposed, such as the two and three diodes (Khanna et al., 2015), but the SD model is the least complex, preserving computational efficiency and being widely disseminated in the photovoltaic community (Baig et al., 2020). The equation for the SD model relates the current (I) and the output voltage (V) of the generator. However, its form is implicit and non-linear, from which it is not easy to solve for $I(V)$. Various ways of solving this equation have been proposed, mostly numerical (Fernández et al., 2013). Also, by giving it the form of the transcendental equation, whose solution corresponds to the Lambert-W function, gives an explicit expression $I(V)$ and a solution in the principal real branch of that function (Batzelis et al., 2020; Corless et al., 1996; Iacono and Boyd, 2017). The Lambert-W function has different ways of solving it, such as approximate forms expansion series and numerical (Iacono and Boyd, 2017; Taciuc and Crăciunescu, 2017). Some are already implemented in different programming platforms, such as Python. However, a simulation of the $I(V)$ characteristics based on this equivalent circuit is not possible without first estimating the electrical parameters associated with the generator: photocurrent, diode saturation current, series resistance, shunt resistance and diode ideality factor. This is why an adequate and precise estimation of these electrical parameters (SD model parameters) (Chin et al., 2015) is of vital importance under the different conditions at which PV modules are subjected. Various methods have been proposed to extract these parameters accurately from experimental I-V curves and manufacturer's datasheet measured under standard test conditions (STC) (Abbassi et al., 2018). The types of applied algorithms can group these methods: a) Metaheuristic optimization algorithms, which use an objective function by minimizing the error between the optimized parameters and the experimental I-V curve, among them: Particle swarm optimization (Ye et al., 2009), Artificial Neural Network (Zhang, 2021), Artificial Bee Colony (Garoudja et al., 2015), Bee Pollinator Flower Pollination algorithm (Alam et al., 2015), simulated annealing (El-Naggar et al., 2012), etc (Chin et al., 2015; Abbassi et al., 2018; Montes-Romero et al., 2018; Yang et al., 2020; Gu et al., 2023; Li et al., 2020; Kharchouf et al., 2022; Ali et al., 2023). b) Numerical algorithms, which can be based on the least squares fitting method (Taciuc and Crăciunescu, 2017), Newton Raphson multivariate (Abdulrazzaq et al., 2020; Ghani et al., 2014; Mlazi et al., 2024), explicit solutions by the Lambert-W function (Cubas et al., 2014), among others. c) Analytical methods, on the other hand, have shown high precision and, in turn, simplicity of implementation and low computational cost, many of which are summarized in Khan et al. (2021), which showed the limitations and validity of the assumptions of the vast number of these methods. Ruschel et al. (2021) reviewed the dependence of the parameters extracted from an SD model on irradiance and temperature under controlled indoor conditions. However, various influences are present under actual operating conditions, such as cloudiness, diffuse irradiance, low light behavior, spectral mismatch, and shadowing (Schweiger et al., 2017). Therefore, the extracted parameters' characteristics and even the applicability of these methods under different outdoor measurement conditions are still an open matter of discussion.

Fernández et al. (2016) carried out a comparative study of the methods by Phang et al. (1984), De Blas et al. (2002), and Khan et al. (2013) to extract the electrical parameters, chosen mainly for their computational simplicity and speed of implementation among the different analytical methods. That comparison was based on experimental data from concentrator photovoltaic (CPV) technology. Since the latter study was conducted for a few experimental curves, Montes-Romero et al. (2018) included one-year data of I- V curves for CPV and c-Si technologies. In this way they obtained a distribution of the accuracy of the three aforementioned methods in addition to the sensitivity analysis against the most influential parameters in PV power generation such as irradiance and module temperature. Nevertheless, a research gap exists in verifying the accuracy and reliability of these methods across various outdoor conditions and contrasting them with the reported indoors. For instance, a solar simulator usually emulates the sunlight as a direct and perpendicular beam. However, the real world is much more complex, involving different direct and diffuse irradiance ratios. Despite this, more in-depth analysis involving sky classification in outdoor conditions has not yet been performed, to our knowledge.

The present work has two aims: First, to broaden previous studies regarding the PV module SD parameters outdoors by additionally discerning between clear and cloudy sky conditions. Second, to validate these parameter extraction methods in a yet unstudied, low-latitude site with particular seasonal behavior and uniform overcast conditions during winter. This study carried out a statistical evaluation of a processed dataset of more than 5200 experimental I-V curves in 12 months measured under the Lima's weather in Peru. This dataset considered the I-V curves of silicon PV modules based on Aluminum Back-Surface Field (Al-BSF), Heterojunction with Intrinsic Thin layer (HIT), and amorphous/microcrystalline silicon (a-Si/μc-Si) technologies. Furthermore, the sensitivity of these three methods is statistically evaluated under different irradiance levels and the sky conditions mentioned above.

2. Fundamentals – the SD model

A PV module is an interconnected PV cell arrangement, usually in series and/or parallel (Yousuf et al., 2022). In the transition from the cell to the module, elements such as glass reflections, resistances in interconnections and cabling, and electrical mismatch between cells cause efficiency losses (Yousuf et al., 2022; Shen et al., 2020) and influence the extracted parameters. Nevertheless, in a simplified way, the modeled PV module can be seen as a collection of interconnected cells neglecting the losses above.

Fig. 1 shows the equivalent circuit representing the SD model. The circuit consists of a current generator connected in parallel with a diode. Shunt and series resistances are added to consider electrical losses, such as those due to grown-in bulk material defects, cracks, technological faults, and contact and material resistances, among others (Breitenstein et al., 2004, 2005; Frühauf and Breitenstein, 2017). Finally, a load R_L is connected in parallel to the end of the circuit where the useful power is consumed.

$$I = I_{ph} - I_0\left[\exp\left(\frac{V+IR_s}{nV_t}\right) - 1\right] - \frac{V+IR_s}{R_{sh}} \tag{1}$$

Eq. 1 represents the equivalent circuit of the SD model in Fig. 1, being an implicit, non-linear expression that relates current and voltage through five electric parameters.

Where the thermal voltage (V_t) can be calculated as shown in Eq. 2, where K_B is the Boltzmann constant, q is the electron charge and T is the PV cell temperature in Kelvin (Shockley, 1953).

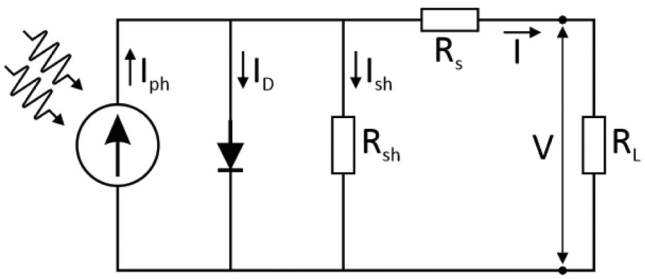

Fig. 1. Equivalent circuit of a cell in the SD model.

$$V_t = \frac{k_B T}{q} \tag{2}$$

In Eq. 1, the photocurrent (I_{ph}) represents the total current generated by the photovoltaic effect. The diode saturation current (I_0) indicates recombination processes for a solar cell. The series resistance (R_s) takes into consideration electric losses due to resistance in the electric contacts, whereas the shunt resistance (R_{sh}) is impacted by leakage currents. Finally, the diode ideality factor (n) measures the junction quality and the type of recombination in a solar cell (Khan et al., 2013; Breitenstein, 2014; Braid, 2019; Steingrube et al., 2011). Each provides valuable information on the physical processes inside the PV cell and can help identify the strengths and weaknesses of PV cells.

The validity of these interpretations for electrical parameters in a PV module is subjected to other additional mechanisms mainly related to outdoor exposure (Fahim et al., 2022). However, as Ruschel et al. (2021) discussed, extracted parameters' behavior exhibited a general trend under the principal influencing factors such as irradiance and temperature, which, in turn, affect the modeling of a PV module. Taking into account that Eq. 1 models the *I-V* curve of a PV module, we reduce its parameters to that of a single representative PV cell (module to cell: *mtc*) following the approach of Eqs. 3 – 7 (Al Tarabsheh et al., 2017; Tian et al., 2012):

$$R_{shunt}^{mtc} = R_{sh} \times (N_p/N_s) \times S \tag{3}$$

$$R_{series}^{mtc} = R_s \times (N_p/N_s) \times S \tag{4}$$

$$J_{dark}^{mtc} = I_0/(N_p \times S) \tag{5}$$

$$n^{mtc} = n/N_s \tag{6}$$

$$I_{ph}^{mtc} = I_{ph}/N_p \tag{7}$$

Where, N_s and $N_p > 1$ indicate the number of cells interconnected in series and parallel, respectively, and S represents the solar cell area. We interpreted this information from the data sheets and from visually inspecting the PV modules.

3. Experimental and methodology

3.1. Experimental setup and data acquisition

The data analyzed in this work was obtained in the Photovoltaic Research Laboratory, as depicted in Fig. 2, installed in the Physics Section of the Pontificia Universidad Católica del Perú (Conde Mendoza et al., 2019). It is located in the coastal area of Lima city (latitude 12°4'S, longitude 77°4'W). The findings reported herein represent the initial mid-term study conducted by this laboratory, which is distinguished as the premier institution in the country equipped with such a diverse range of apparatuses for the outdoor characterization of PV modules.

The PV modules are facing north at a 20° tilt angle. This tilt angle favors the reduction of dust accumulation despite not being optimal regarding irradiation received. The *I-V* curve tracer is based on a capacitive load as described in Montes-Romero et al. (2017) and showed very low uncertainties, around 0.58 % and 0.23 % for the I_{sc} and V_{oc}, respectively (Cáceres et al., 2020). Two digital multimeters, Keysight 34465 A, measure the *I-V* curve of each PV module, lasting from 2 to 40 s depending on the current of the PV technology and irradiance level. Measurements of the broadband irradiances (Global Horizontal Irradiance, GHI, and plane-of-array irradiance, G_{poa}) are performed with two EKO MS-80 pyranometers. An EKO MS711 spectroradiometer captures the spectral irradiance. From this spectral data, we calculate the Average Photon Energy (APE) in the range of 350–1050 nm, as described in (Sevillano-Bendezú et al., 2022). This index indicates the blueness and redness of actual solar spectra relative to the AM1.5 G spectrum ($APE_{AM1.5G} = 1.876$ eV) (Sevillano-Bendezú et al., 2022, 2023; Jardine et al., 2002; Williams et al., 2003).

The module's temperature (T_{module}) is the average value of the temperatures measured with two PT100 class B sensors at the rear side center and corner. The *I-V* curves for each PV module were measured every 5 minutes, synchronously with all ambient parameters. Additionally, the modules were cleaned weekly to minimize soiling effects.

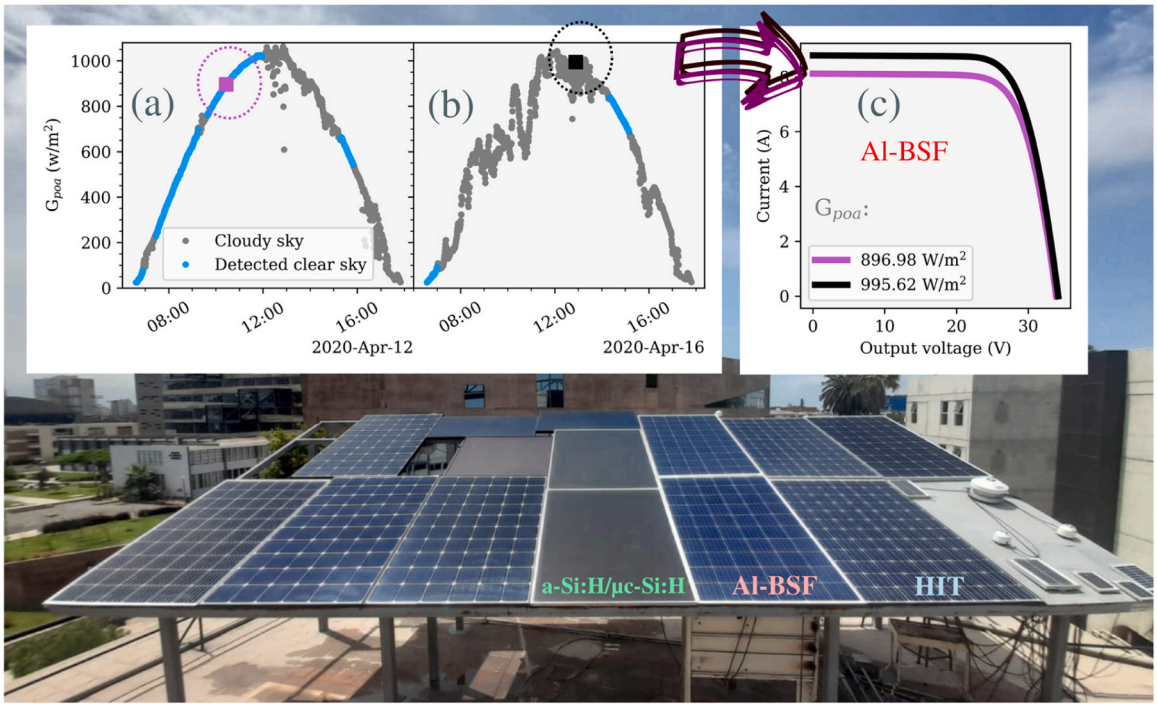

Fig. 2. Photovoltaic Research Laboratory highlighting the studied PV technologies: Al-BSF, HIT and for a-Si:H/µc-Si:H. Insets plots show two exemplary days with detected (a) clear, and (b) cloudy sky irradiances, and (c) two *I-V* curves taken from both sky conditions for the Al-BSF PV module.

More details on the PV module characterization system and its components are described in (Conde Mendoza et al., 2019).

This study selected three different PV technologies: p-type multicrystalline silicon Al-BSF, n-type mono-crystalline HIT, and a tandem based on a-Si/μc-Si. The electrical characteristics of the PV modules in STC conditions extracted from the datasheet are shown in Table 1.

We followed the subsequent procedures for measuring and preprocessing the data sets:

- The irradiance was measured at the beginning and end of the *I-V* curve tracing. To eliminate curves with varying irradiance during tracing, only *I-V* curves were considered when the relative difference between these two irradiances was lower than 4 %.
- We adapted the Data-Driven *I-V* Feature extraction (ddiv) package implemented in the R programming language (Ma et al., 2019) to identify and discard *I-V* curves with shading steps or other electrical current drops from any other malfunctions.
- We handled all further preprocessing of *I-V* curves and computation of additional parameters with Python, such as the Angle of Incidence (*AoI*) and the Clear Sky Index (Holmgren et al., 2018). The preprocessing steps included:
  - To reduce the noise in the measured *I-V* curves, we applied the Savitzky–Golay filter using Python on each curve. This filter facilitated the identification of stepped *I-V* curves using the ddiv algorithm.
  - Filtering the dataset to discard *I-V* curves with an $AoI > 50°$, thus decreasing angular effects in the final dataset.
  - We implemented the Reno-Hansen algorithm (Reno and Hansen, 2016) to detect clear sky instantaneous events. In this step, we assume that the instants in which the irradiance behaves smoothly and coincide with the usual bell shape that the irradiance has in a clear sky qualify as a time instant of a clear sky; otherwise, we assume that it is not a clear sky as shown in the inserted plots (a) and (b) in Fig. 2. Insert (c) shows two exemplary *I-V* curves corresponding to instants of clear and cloudy sky for the Al-BSF PV module. The algorithm is described in detail in Reno and Hansen (2016), for which we input GHI irradiance measurements and the simulated clear sky irradiance by REST2 (Gueymard, 2008) readily available in the National Solar Radiation Database (NSRDB) (Sengupta et al., 2018). However, we additionally made a visual inspection to correct those instants corresponding to the *I-V* curve measurements that were not well identified by the clear sky detection algorithm.
  - The *I-V* curves were broken down into ten groups of varying irradiance, going from 100 to 1000 W/m^2 in steps of 100 W/m^2. Each group allowed *I-V* curves with an irradiance tolerance of ± 5 W/m^2, e.g., from 95 to 105 W/m^2 for the first group and so on.

After applying the preprocessing steps described above, the final dataset, including the three PV modules, consisted of over 5200 *I-V* curves from June 2019 to May 2020 (See Fig. A1 in Appendix A).

Table 1
Electrical characteristics of the PV modules at STC.

Electrical Parameters	Al-BSF	HIT	a-Si/μc-Si
Maximum Power in W	270	330	128
Short-circuit current (I_{sc}) in A	9.32	6.07	3.45
Open-circuit voltage (V_{oc}) in V	37.9	69.7	59.8
Temperature coefficient for I_{sc} in mA/C° (—in %/C°, $\alpha_{I_{sc}}$)	4.93 (0.053)	3.34 (0.055)	2.42 (0.070)
Temperature coefficient for V_{oc} in V/C° (—in %/C°, $\beta_{V_{oc}}$)	−0.12 (−0.31)	−0.16 (−0.24)	−0.18 (−0.30)
Temperature coefficient for the maximum power in %/C°, $\gamma_{P_{max}}$	−0.410	−0.258	−0.240

3.2. Analytical extraction methods

The analytical methods chosen in the present work are easy to implement and exhibit high accuracy at mid-latitude and in a sunny climate (Montes-Romero et al., 2018). These methods require three key points of the *I-V* curve: the short circuit current, I_{sc}, the open circuit voltage V_{oc}, and the current and voltage at the maximum power point, I_{mpp}, and V_{mpp}, respectively. Additionally, initial estimated values for the shunt and series resistances are required. They correspond to the inverse of the curve's slope at the I_{sc} and V_{oc} points; these are called R_{sho}, and R_{so}, as expressed by Eqs. 8 and 9, respectively.

$$R_{sho} = -\left[\frac{dV}{dI}\right]_{I=I_{sc}} \tag{8}$$

$$R_{so} = -\left[\frac{dV}{dI}\right]_{V=V_{oc}} \tag{9}$$

To obtain R_{so} and R_{sho}, we used a couple of linear fits on the edges of the *I-V* curve. The fit for R_{so} was applied to data points ranging from 0 % to 40 % of the I_{mpp}, while the fit for R_{sho} was applied to data points with voltage values within the 0–65 % V_{mpp} range. The negative inverse values of the slope are then used as the values for R_{so} and R_{sho} as seen in Fig. 3.

The three analytical methods are described below.

Method by Phang et al. (1984):

This method provides five equations so that each electrical parameter can be calculated using the key values of the *I-V* curve described above. The equations can be arranged, so there is no need to solve a system of simultaneous equations.

$$R_{sh} = R_{sho} \tag{10}$$

$$n = \frac{V_{mpp} + R_{so}I_{mpp} - V_{oc}}{V_t\left[\ln\left(I_{sc} - \frac{V_{mpp}}{R_{sh}} - I_{mpp}\right) - \ln\left(I_{sc} - \frac{V_{oc}}{R_{sh}}\right) + \frac{I_{mpp}}{I_{sc} - \frac{V_{oc}}{R_{sh}}}\right]} \tag{11}$$

$$I_0 = \left(I_{sc} - \frac{V_{oc}}{R_{sh}}\right)\exp\left(-\frac{V_{oc}}{nV_t}\right) \tag{12}$$

$$R_s = R_{so} - \frac{nV_t}{I_0}\exp\left(-\frac{V_{oc}}{nV_t}\right) \tag{13}$$

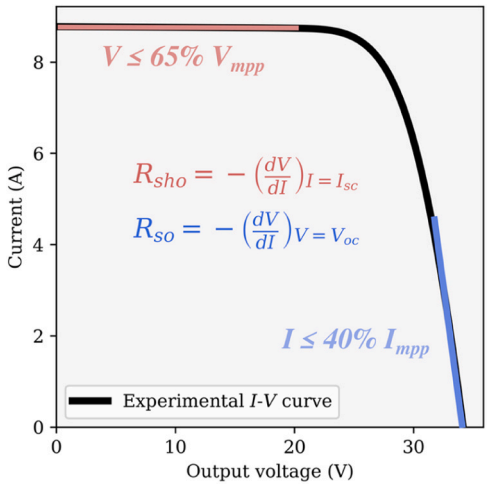

Fig. 3. Exemplary experimental *I- V* curve at 1000 W/m2 with schematic linear fits near I_{sc} and V_{oc} to estimate initial values R_{so} and R_{sho}, respectively.

$$I_{ph} = I_{sc}\left(1+\frac{R_s}{R_{sh}}\right)+I_0\left(\exp\left(\frac{I_{sc}R_s}{nV_t}\right)-1\right) \tag{14}$$

Method by De Blas et al. (2002):

This method requires an initial estimate for R_s. The values for R_{sh} and n are then estimated using the initial R_s through Eqs. 15 and 16. In this study, R_{so} was introduced as an initial value for R_s. After this, the series resistance can be recalculated using Eq. 17, and this new result is used to recalculate R_{sh} and n. After R_s converges, the method provides a couple of Eqs. 18 and 19 for calculating I_0 and I_{ph}, respectively.

$$R_{sh} = R_{sho} - R_s \tag{15}$$

$$n = \frac{V_{mpp}+R_{so}I_{mpp}-\mathrm{V}_{oc}}{V_t \ln\left[\frac{\left(\mathrm{I}_{sc}-I_{mpp}\right)\left(1+\frac{R_s}{R_{sh}}\right)-\frac{V_{mpp}}{R_{sh}}}{I_{sc}\left(1+\frac{R_s}{R_{sh}}\right)-\frac{\mathrm{V}_{oc}}{R_{sh}}}\right]} \tag{16}$$

$$R_s = \frac{R_{so}\left(\frac{\mathrm{V}_{oc}}{nV_t}-1\right)+R_{sho}\left(1-\frac{\mathrm{I}_{sc}R_{so}}{nV_t}\right)}{\frac{\mathrm{V}_{oc}-\mathrm{I}_{sc}R_{sho}}{nV_t}} \tag{17}$$

$$I_0 = \left(I_{sc}\left(1+\frac{R_s}{R_{sh}}\right)-\frac{\mathrm{V}_{oc}}{R_{sh}}\right)\exp\left(-\frac{\mathrm{V}_{oc}}{nV_t}\right) \tag{18}$$

$$I_{ph} = I_0\left(\exp\left(\frac{\mathrm{V}_{oc}}{nV_t}\right)-1\right)+\frac{\mathrm{V}_{oc}}{R_{sh}} \tag{19}$$

Method by Khan et al. (2013):

This method uses Phang's Eq. 10 for the shunt resistance and Eq. 19 for the photocurrent. Then it provides its equations to extract the remaining parameters.

$$R_s = R_{so} - \frac{V_{mpp}+R_{so}I_{mpp}-\mathrm{V}_{oc}}{I_{mpp}+\left(\ln\left(I_{sc}-I_{mpp}\right)-\ln(\mathrm{I}_{sc})\right)\mathrm{I}_{sc}} \tag{20}$$

$$I_0 = \frac{nV_t}{R_{so}-R_s}\exp\left(-\frac{\mathrm{V}_{oc}}{nV_t}\right) \tag{21}$$

$$n = \frac{V_{mpp}+R_sI_{mpp}-\mathrm{V}_{oc}}{V_t\left(\ln\left(\mathrm{I}_{sc}-I_{mpp}\right)-\ln(\mathrm{I}_{sc})\right)} \tag{22}$$

Phang et al. assume that R_{sh} is much larger than R_s. However, such an approximation may vary depending on the PV technology and quality of the PV generator. Since a degraded module presenting a considerably high R_s could reduce the validity of this approximation. De Blas et al. present two essential limitations despite the advantage of introducing fewer assumptions than the other two methods: First, an arbitrary initial value of R_s must be taken to calculate R_{sh}, n, and I_0. That means knowing a priori an estimate of R_s. Second, the convergence of the iterative method depends on this initial value. Khan et al. assume that R_{sh} is much larger than R_s, as Phang et al. assumed. Additionally, Khan et al. extend their method validity to very high irradiances, even higher than 10 suns, by making ad-hoc assumptions (Khan et al., 2021). While such assumptions broaden the scope of application regarding irradiance, they do not guarantee accuracy comparable to that of the other methods under all illumination conditions.

3.3. Accuracy evaluation

To compare the applicability of these three analytical methods, once we extracted the electrical parameters, they were used to simulate a theoretical *I-V* curve. We simulate the *I-V* curve using the W-Lambert method from Python pvlib (Holmgren et al., 2018). The theoretical curve based on the extracted parameters is compared with the experimental one through the normalized root mean square error (NRMSE) as in Montes-Romero et al. (2018) and the absolute error used in Arabshahi et al. (2020) as follows:

$$\mathrm{NRMSE} = 100\% \times \sqrt{\frac{1}{N}\sum_{j=1}^{N}\left(\frac{I_{theoretical}(V)_j - I_{experimental}(V)_j}{\mathrm{I}_{SC,experimental}}\right)^2} \tag{23}$$

$$Absolute\ error(V)_j = \left|I_{theoretical}(V)_j - I_{experimental}(V)_j\right| \tag{24}$$

Where, $I_{theoretical}$ and $I_{experimental}$ represent the simulated and experimental current, respectively, index j is associated with a specific current-voltage tuple $I(V)_j$ in the experimental and the theoretical *I-V* curves, N is the total number of points for each of these curves. Finally, $I_{SC,experimental}$ expresses the experimental short circuit current of the examined curve.

4. Results and analysis

4.1. The sky of Lima through the Clear Sky Index

Lima is characterized by its uniformly cloudy skies with layers of stratus clouds, especially in the winter months from June to September, as reported by Enfield (1981). During these winter months, we observe relatively low monthly Clear Sky Index values below 0.55, as seen in Fig. 4. The monthly irradiance-weighted Clear Sky Index indicates that in average measured irradiances are up to 55 % below the ones predicted by the NSRDB Clear Sky modeled GHI. The instantaneous Clear Sky Index values have relatively low dispersion. In contrast, less cloudiness is exhibited in the summer and first autumn months from December to April with monthly Clear Sky Index values close to 1.0. The instantaneous values are highly dispersed. It should be noted that the modeled data has not been site adapted (Polo et al., 2016). However, it showed a better approximation than the data modeled by pvlib (Holmgren et al., 2018) (not shown here).

The heat map in Fig. 5 shows the most frequent conditions depending on the Clear Sky Index and G_{poa} during the twelve months of the experimental campaign. The data concentrates at two ranges: One high percentage of data corresponds to G_{poa} of around (900–1000) W/m^2 and a Clear Sky Index of around 1, i.e., for a clear sky. Another high data percentage is given for low irradiances around (100−300) W/m^2 and Clear Sky Index between 0.2 and 0.3, indicating a low sky clearness for a cloudy sky. Note that limiting the analyzed data to $AoI < 50^\circ$ filters out data for G_{poa} below approximately 500 W/m^2 with Clear Sky Index of around 1.

4.2. Performance parameters analysis

Under Lima's local specific conditions described above, we study the behavior of the main performance parameters. The variation of these parameters also influences the reliability of the parameter extraction by analytical methods since the assumptions' limitations of these methods generally depend on performance parameter relationships (Khan et al., 2021).

Fig. 6 demonstrates the performance parameters obtained from 12 months of *I-V* curve measurements of the three PV modules. We calculated I_{sc}^{T-corr} by dividing I_{sc} by the factor $[1+\alpha_{I_{sc}} \times (T_{\mathrm{mod}} - 25^\circ\mathrm{C})]$. We analyzed the parameters' dependence on the main physical factors affecting them, differentiating between clear and cloudy sky conditions. Fig. 6(a) shows the linear relationship between I_{sc}^{T-corr} and G_{poa}. I_{sc}^{T-corr} under clear skies presents less dispersion than under cloudy skies, indicating that the latter causes higher uncertainties in the I_{sc}^{T-corr} and its measurement. Fig. 6(b) shows the I_{sc}^{T-corr} vs. *AoI* relationship. Under a clear sky, a markedly decreasing trend is observed for all technologies. This evidences the relation of the irradiance with the *AoI* in clear skies, in addition to verifying the proper functioning of the clear sky detection algorithm. For cloudy skies, there is no evident dependence of the I_{sc}^{T-corr} on the *AoI*, indicating that I_{sc}^{T-corr} is predominantly generated by the *AoI*-

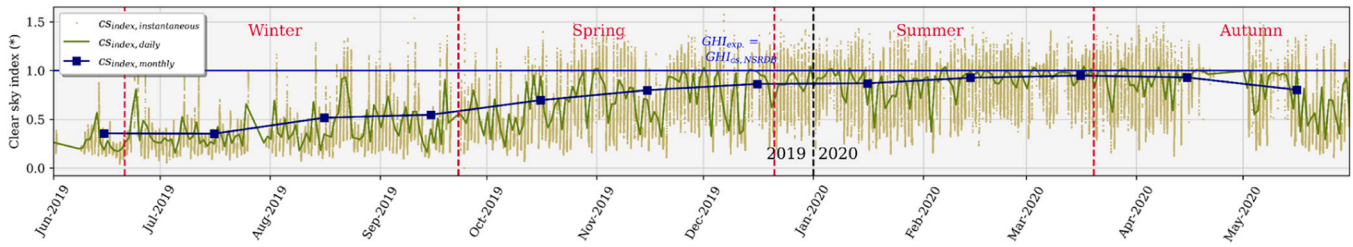

Fig. 4. Clear Sky Index (cs_{index}) time series in instantaneous, daily, and monthly time scales divided by seasons. The daily and monthly values result from averaging the instantaneous values weighted to irradiance.

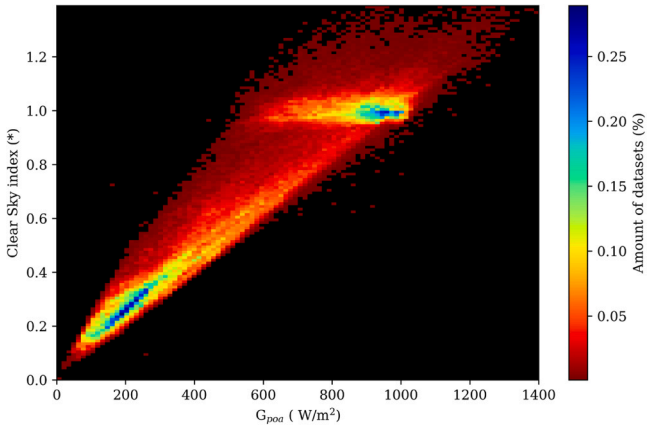

Fig. 5. Heat map showing the percentual number of datasets by G_{poa} and the Clear Sky Index for $AoI < 50°$ from June 2019 to May 2020.

independent diffuse irradiance component. In Fig. 6(c), the APE is mainly above the $APE_{AM1.5G}$; therefore, the spectral distribution is shifted predominantly to blue. The *APE*, however, does not show an evident correlation with the I_{sc}^{T-corr} for the c-Si-based technologies (HIT and Al-BSF). Considering that in Lima's *APE* range, the performance variation for these technologies in terms of spectral mismatch factor is below 2 %, as we demonstrated in (Conde et al., 2021), it is reasonable to assume that this low impact of the APE is within the dispersion of I_{sc}^{T-corr} in Fig. 6(c). In the case of the a-Si/μc-Si tandem module, no impact of the APE on the I_{sc}^{T-corr} is evident as well, which could be attributed to the bottom subcell limiting the current of the tandem cell for the blue-shifted spectra. However, Fig. 6(c) demonstrates that the blue-shifted spectra with higher APE are primarily associated with cloudy sky conditions, consistent with our observation of spectral blue-shift under cloudy conditions in Lima, as reported in (Zamalloa-Jara et al., 2023). In Fig. 6 (d), the *FF* generally shows a decreasing trend with higher irradiance. In addition, the HIT module maintains at high irradiances a higher *FF* than the other PV technologies. However, such a trend does not show appreciable distinction in the clear and cloudy skies, except for the lower dispersion of the *FF* for clear sky conditions. Fig. 6(e) shows the V_{oc} and module temperature relationship. We observe the decreasing trend associated with the temperature increase influencing the bandgap's reduction, which drives a smaller V_{oc} when module temperature increases (Dupré et al., 2015). This relationship becomes noticeably linear under clear-sky conditions. By making a linear regression for irradiances around 1000 W/m^2 and under clear skies, we obtain slopes about −0.11, −0.15, and −0.17 V/°C for the Al-BSF, HIT and a-Si/μc-Si tandem modules, respectively. These slopes express the PV modules' temperature coefficients and are close to those in the manufacturer's datasheet in Table 1, exhibiting a deviation up to −0.01 V/C°.

4.3. Extracted parameters of PV modules: Representative single PV cell

Fig. 7 depicts the trends with the irradiance of the parameters reduced to a representative cell extracted by the three analytical methods Phang et al. (1984), De Blas et al. (2002), and Khan et al.

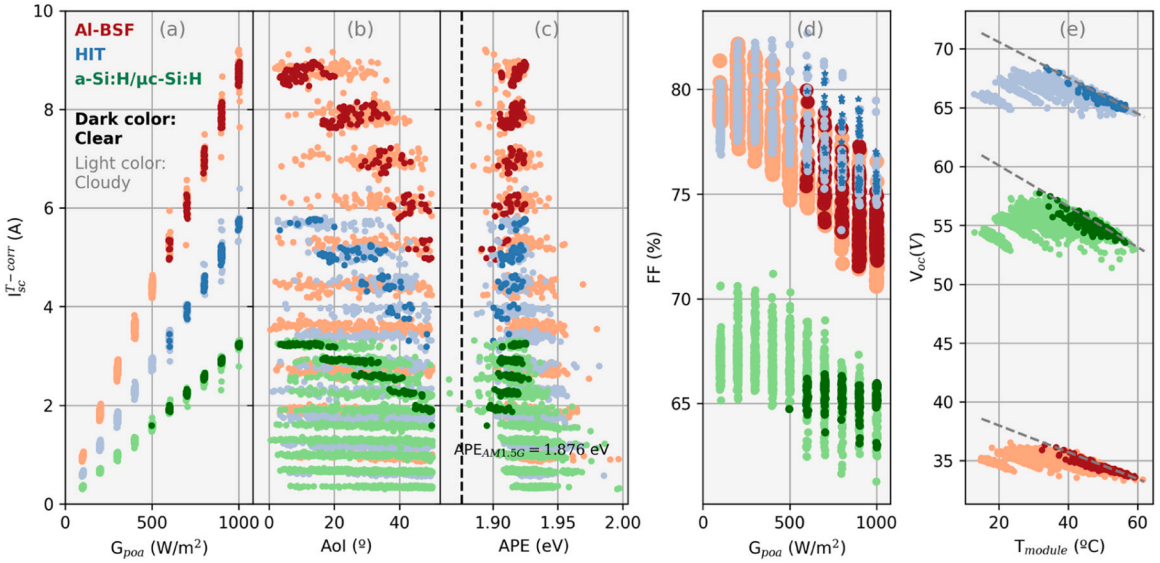

Fig. 6. Performance indicators' relationships with the most influential physical factors in clear and cloudy sky conditions obtained from 12 months of *I-V* curves: Temperature-corrected Short Circuit Current (I_{sc}^{T-corr}) as a function of (a) G_{poa} levels. (b) the *AoI*, and (c) the *APE*. (d) *FF* as a function of G_{poa} levels, and (e) V_{oc} depending on T_{module}. Dashed lines represent the linear regression for clear sky data and irradiances around 1000 W/m^2.

(2013) in all sky conditions. All three methods yield extracted parameters with similar values and trends. For Al-BSF and HIT R^{mtc}_{shunt} is higher than that of the a-Si/μc-Si tandem, although more dispersed at lower irradiances. This is most likely related to the Si bulk-based PV modules' lower amount of bulk and surface defects (Belghachi and Limam, 2017; Merten et al., 1998; Phillips et al., 2020; Sandberg and Armin, 2019).

For all methods and technologies, we observe a decrease of R^{mtc}_{shunt} with irradiance and a stabilization above 600 W/m^2. Similar behavior has been reported earlier in Montes-Romero et al. (2018), Ruschel et al. (2021); De Soto et al. (2006), Schroder (2005), Ramesh et al. (2022). In the case of R^{mtc}_{series}, we observe lower values for the Al-BSF and HIT technologies than for the a-Si/μc-Si tandem, probably due to the higher conductivity of the semiconductor layers of these technologies (Yoon et al., 2015; Sturiale et al., 2009). In all technologies, the R^{mtc}_{series} decreases with irradiance intensity. The R^{mtc}_{series} decreasing with illumination has also been reported previously in Montes-Romero et al. (2018), Ruschel et al. (2021), Stein et al. (2014) and attributed to higher photo-generated charge carrier density at higher irradiances, which in turn probably increases the conductivity of the semiconductor layers (Montes-Romero et al., 2018).

Regarding n^{mtc}, we observe mean values between 1.0 and 1.5 for the Al-BSF and HIT technologies and about 2.0 for the a-Si/μc-Si when applying the Phang et al. and de Blas et al. methods. These values are slightly higher when employing the Khan et al. method. On the one hand, n^{mtc} is algebraically sensitive to the PV module temperature uncertainties (Eq. 1); however, it remains almost constant for the different irradiance levels. On the other hand, a diversity of values for the diode ideality factor has been reported previously (Riben and Feucht, 1966; Padovani and Stratton, 1966; Rau et al., 2000) while theoretically ranging between 1 and 2 (Sah et al., 1956; Zhu et al., 2009; Caprioglio et al., 2020; Mcintosh et al., 2000); thus, the SD model has a wide range of interpretations regarding this parameter, especially for thin-film PV technologies (Rau et al., 2000; Mcintosh et al., 2000; Breitenstein et al., 2006). At the same time, J^{mtc}_{dark} extracted by the analytical methods does not seem to show a clear trend in the logarithmic scale. However, when compared to the Al-BSF and HIT, the higher J^{mtc}_{dark} values for the a-Si/μc-Si tandem module are consistent with what would be expected regarding the more significant non-radiative recombination losses (higher J^{mtc}_{dark}) due to the technologies higher material defect densities (Meillaud et al., 2009). No significant distinction between Al-BSF and

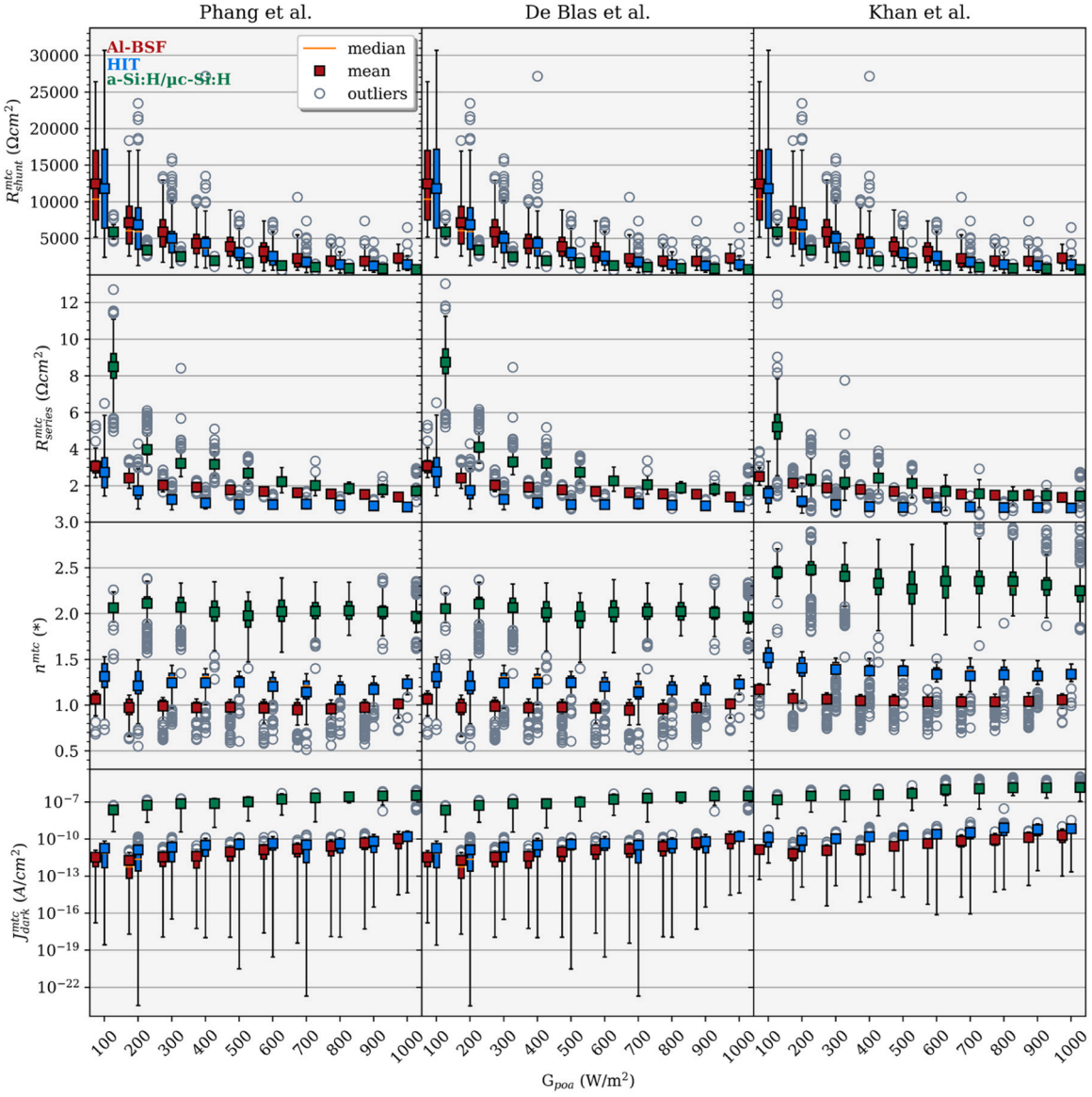

Fig. 7. Box plot for the four principal extracted parameters R^{mtc}_{shunt}, R^{mtc}_{series}, n^{mtc}, and J^{mtc}_{dark} for different G_{poa} levels at all-sky conditions. The superscript *mtc* expresses the parameter reduction from PV module to cell according to Eqs. 3 – 6.

HIT modules can be made in terms of J^{mtc}_{dark}.

The trends presented in this work for crystalline silicon-based PV modules, primarily for R^{mtc}_{shunt} and R^{mtc}_{series} extracted from all-sky condition measurements, are consistent with those reported before in outdoor exposure (Montes-Romero et al., 2018). In addition, the three methods evaluated preserve both the trends and the rough numerical comparisons of these parameters between different technologies. However, the most significant difference between these three methods is in the absolute values of the extracted parameters. Thus, this analysis represented a qualitative validation of the extracted parameters.

Fig. 8 allows a more in-depth analysis of the extracted parameters, discriminating them by sky condition (clear and cloudy) and irradiance level. This figure shows the trends of the extracted parameters under clear skies for irradiances above 600 W/m^2. We identified no considerable differences between clear and cloudy skies for R^{mtc}_{shunt} in this irradiance range. At 600 W/m^2, there is an apparent separation of the R^{mtc}_{shunt}'s irradiance trends for all three PV technologies, with slightly lower R^{mtc}_{shunt} values under clear-sky conditions. The cell temperatures under cloudy sky conditions tend to be lower than under clear-sky, and their difference becomes more pronounced at the mid-range irradiances, as seen in our data (not shown here). The impact of the cell temperature on the *FF*, and thus on R^{mtc}_{shunt} and R^{mtc}_{series}, has been studied for c-Si technologies under laboratory conditions, indicating a drop in the *FF* at higher cell temperatures (Haschke et al., 2017). Here, however, this assessment is limited to the mid-range irradiances due to the lack of clear-sky outdoor data at lower irradiances. Nevertheless, the observed difference in R^{mtc}_{shunt} between clear and cloudy sky conditions could be related to the cell temperature difference at around 600 W/m^2. The R^{mtc}_{series} of the Al-BSF and HIT modules show no evident distinction between clear and cloudy sky for the irradiance range above 600 W/m^2. However, for the a-Si/µc-Si tandem module, the R^{mtc}_{series} values under clear skies are slightly lower than under cloudy skies, indicating that the thin-film tandem technology may be more prone to changes in the direct/diffuse irradiance ratio and/or to cell temperature differences in the mid irradiance range. Furthermore, we observe for the a-Si/µc-Si tandem module that the R^{mtc}_{series} at clear skies remains constant when extracted by Phang et al. and De Blas et al. methods but shows an increasing trend towards lower irradiances when applying the Khan et al. method. We highlight that the Khan et al. method for the tandem module exhibits an increasing absolute error with increasing irradiance

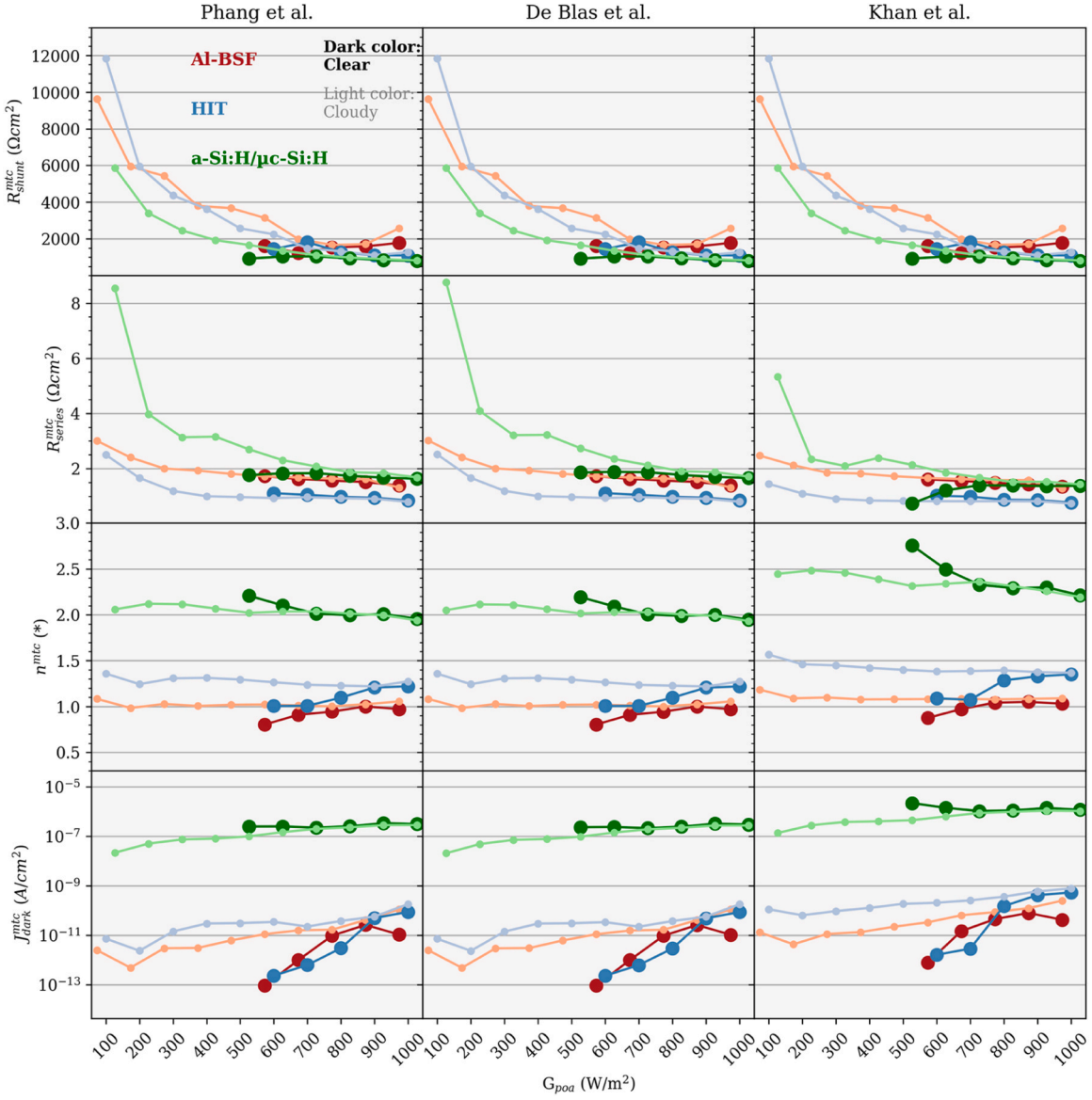

Fig. 8. Mean values for the four principal extracted parameters R^{mtc}_{shunt}, R^{mtc}_{series}, n^{mtc}, and J^{mtc}_{dark} for different G$_{poa}$ levels distinguishing between clear (dark color) and cloudy (light color) sky conditions.

near V_{oc}, unlike the other two methods, where the absolute error near V_{oc} remains almost constant (Fig. A3 in Appendix A). Therefore, such variable errors may influence the above trend of R_{series}^{mtc} in the a-Si/µc-Si tandem module.

The parameters n^{mtc} and J_{dark}^{mtc} for the Al-BSF and HIT modules show a trend that depends on the sky condition. Surprisingly, under clear skies, n^{mtc} and J_{dark}^{mtc} increase with irradiance, similar to that reported for crystalline silicon-based technologies in different exhaustive analyses under controlled laboratory conditions (Ruschel et al., 2021; Hali and Khlifi, 2022; Chegaar et al., 2013). While under cloudy skies, the mean of these parameters remains almost constant. Under clear skies, the direct irradiance is greater than the diffuse component in the measured global irradiance. This assumption is consistent with the *AoI* filter that discards curves subject to irradiances in early mornings and late afternoons, where angular effects become more relevant (Schweiger et al., 2017) and global irradiance has a higher diffuse component. Therefore, increasing n^{mtc} and J_{dark}^{mtc} with irradiance level under clear skies could come from the increased direct component getting closer to what can be simulated in a laboratory. Likewise, cloudy sky irradiances present a more prominent diffuse component than under a clear sky. In the present work, we see that Al-BSF and HIT modules under cloudy skies exhibit larger n^{mtc} and J_{dark}^{mtc}, influencing the recombination mechanisms at the cell level (Mialhe et al., 1986). Interestingly, the a-Si/µc-Si tandem module demonstrates a behavior opposite to the previous modules under clear skies. This fact, in combination with the almost constant behavior of R_{shunt}^{mtc} and R_{series}^{mtc}, would explain the lack of a defined trend for their *FF* at different irradiance levels under clear skies in Fig. 6. The *FF* decreasing trend under cloudy skies in Fig. 6 for the three technologies seems to be dominated by the R_{shunt}^{mtc} decreasing trend over the other parameters' trends. The changes in *FF* in the *I-V* curves for different sky conditions are shown in Fig. A2 In the Appendix A.

4.4. SD model parameters' extraction methods comparison

Since the three methods studied reproduce trends, validating their accuracy is necessary to distinguish qualitatively between them.

Fig. 9 shows the extraction methods' accuracy in reproducing the *I-V* curve under clear and cloudy skies. More dispersion and outliers are observed under cloudy skies than under clear skies. This could be due to a propagation of the above-mentioned lower dispersion of the performance parameters under clear skies over the extracted parameters. For Phang et al. and de Blas et al., the NRMSE also seems to present a mainly

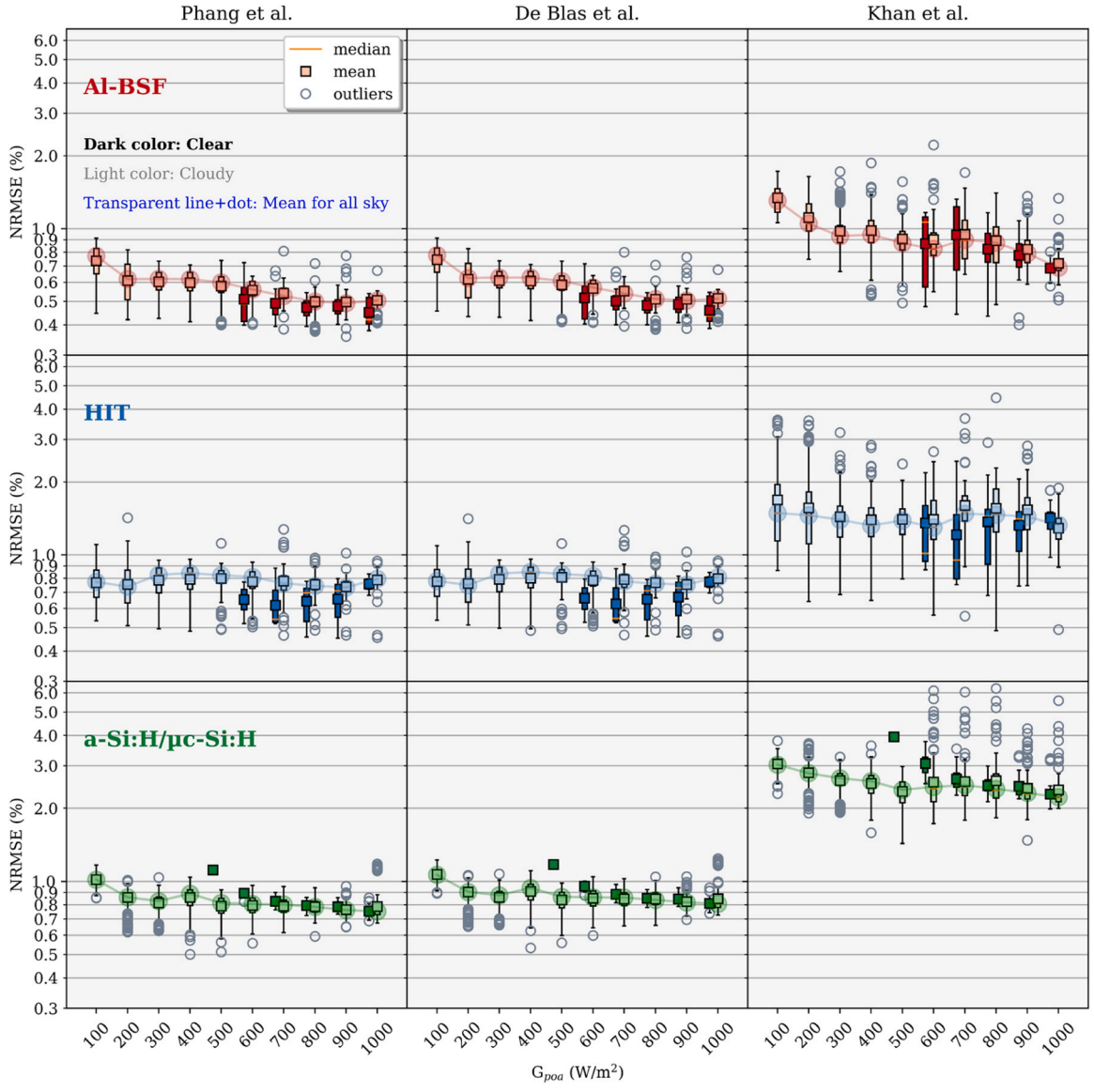

Fig. 9. NRMSE box plots per G_{poa} level split by clear and cloudy sky conditions for Al-BSF, HIT, and a-Si/µc-Si technology.

decreasing trend with irradiance for clear and cloudy skies, as exhibited in the mean value in all-sky conditions represented by the transparent line. The decreasing trend indicated by the mean values under all-sky with irradiance is maintained for the Al-BSF module with the three methods considered. The HIT module seems to remain indifferent under varying irradiance, i.e., the mean NRMSE for the HIT module is stable at different irradiances. In contrast, the a-Si/μc-Si tandem does not present a definite trend.

In addition, a higher dispersion is observed for Al-BSF and HIT modules than for the a-Si/μc-Si tandem. While Phang et al. and Blas et al. show similar results for the three technologies studied, they also exhibit a minor error, i.e., higher precision than Khan et al. method. Interestingly, for all extraction methods, the NRMSEs of the Al-BSF and HIT technologies for clear sky conditions are lower than for cloudy sky conditions at the corresponding irradiances (600 – 1000) W/m^2. However, in the case of the a-Si/μc-Si, the NRMSEs for cloudy and clear sky conditions are statistically indifferent at higher irradiances, and at lower irradiances the NRMSEs for cloudy sky tend towards higher values.

Fig. A3 in Appendix A shows the absolute error (Eq. 24) divided by I_{sc} in absolute value along the output voltage, which shows that such a ratio presents the most significant difference for values close to the maximum power point and V_{oc}. where the absolute error (the difference between the experimental and theoretical currents) proves to be below 4 % of its corresponding I_{sc} for Phang et al., and de Blas et al. for the three PV modules. However, Khan et al. even exceeds 8 % for the a-Si/μc-Si tandem.

Finally, Fig. 10 summarizes the accuracy of the three analytical methods under clear and cloudy skies. The extensive *I-V* curve selection methodology described above contributes to the overall NRMSE values we show by reducing the presence of artifacts in the data set. The results generally exhibit the lowest NRMSEs under clear skies (over 600 W/m^2). However, the NRMSE under cloudy conditions significantly contributes to a higher integrated NRMSE.

In addition, we note that Al-BSF corresponds to the slightest overall error, and Phang et al. and Blas et al. show to be mostly below 1 % for all technologies, while Khan et al. increases above 1 % and even above 2 % for the a-Si/μc-Si tandem. Phang et al. and Blas et al. seem to work similarly for c-Si-based technologies (Al-BSF and HIT), which we also show by having the same confidence interval range. However, for the a-Si/μc-Si tandem, Phang et al. offer the best option under these local conditions due to its slightly lower NRMSE. Therefore, Phang et al. prove to be the most versatile option since it consistently maintains a lower error for all technologies and fewer outliers.

5. Conclusions

This study evaluated the precision of three analytical extraction methods—namely, those developed by Phang et al., de Blas et al., and Khan et al.—focusing on their efficacy in determining the single-diode (SD) parameters of photovoltaic (PV) modules under varying sky conditions: all-sky, clear, and cloudy. The research encompassed three distinct module technologies: Al-BSF, HIT, and a-Si/μc-Si tandem, while also considering key factors influencing their SD parameters, including irradiance level, angle of incidence (AoI), temperature, and the spectral distribution as indicated by the *APE*. The fill factor (*FF*) of the three PV modules demonstrated a decreasing trend with the irradiance level under cloudy conditions, a pattern seemingly governed by the decreasing trend of R_{shunt}^{mtc}. Under clear skies, this pattern was observed only for the Al-BSF and HIT technologies. The variation in extracted parameters with irradiance under all-sky conditions aligns with previously documented outdoor measurement results but deviates from indoor measurement trends. This difference reconciles when considering only clear-sky outdoor data, aligning the trends of outdoor and indoor measurements. This suggests that outdoor conditions, particularly diffuse, cloudy-sky irradiance, may differently affect certain solar cell parameters compared to direct irradiance. Furthermore, by filtering clear-sky conditions, the dispersion of the performance parameters is reduced, thus, lowering the error in obtained the respective parameter under given outdoor-conditions.

For clear sky conditions, the Al-BSF and HIT modules displayed lower NRMSE values in replicating the I-V curve with the extracted parameters, in contrast to the a-Si/μc-Si tandem technology, which showed higher NRMSE under clear skies at 600 W/m^2, with its response to sky conditions becoming invariant with increasing irradiance. Overall, our assessment of these extraction methods confirmed that the approaches of Phang et al. and de Blas et al. yield mean NRMSEs below 1 % for all examined module technologies in replicating the experimental *I-V* curve with the extracted parameters, with even lower mean NRMSEs under clear sky conditions. This high fidelity of the simulated *I-V* curves underscores the reliability of the extracted parameters when considering a SD model.

This work ignores angular influences and evades a more detailed classification of cloudy skies regarding cloud types, such as over-irradiance events. Future work should attempt to resolve these limitations. Additionally, the defined NRMSE provides indirect and reduced insights into the accuracy of the extracted parameters. Therefore, indicators that directly reflect the accuracy of the extracted parameters should be explored.

The methodologies introduced in this paper have potential

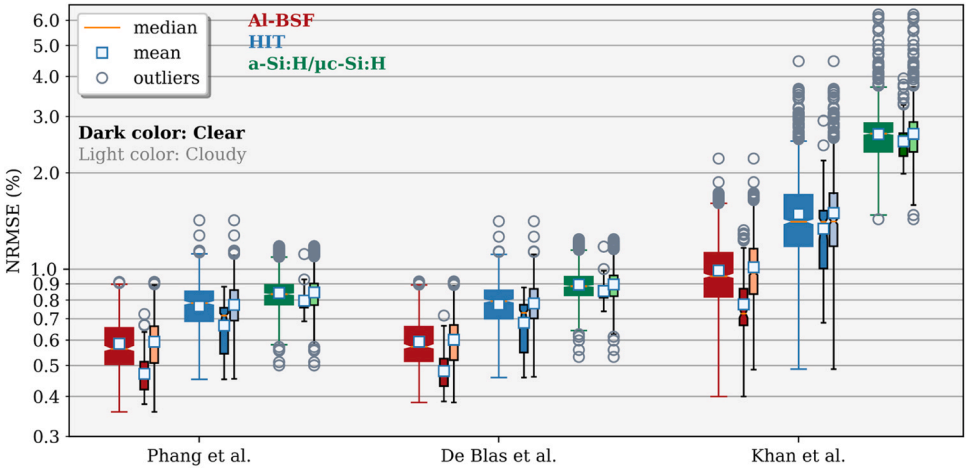

Fig. 10. Integrated (all sky condition), clear and cloudy NRMSE results for each extraction method in notched box plots. Wide box represents all sky condition, narrow boxes distinguish between clear (dark color) and cloudy (light color) sky conditions. Notches indicate the 95 % confidence interval around the median value.

applications in the long-term monitoring of PV module parameters, offering enhanced precision in the extraction of SD parameters under outdoor conditions by distinguishing, for instance, between clear and cloudy skies. Future research focusing on the correlation between irradiance values, sky conditions, and their respective errors will facilitate a deeper understanding of the relationship between operational conditions and their effects on SD and performance parameters. Such in-depth analyses could also illuminate potential degradation mechanisms, as indicated by variations in the extracted parameters.

CRediT authorship contribution statement

Jan Amaru Palomino Töfflinger: Writing – review & editing, Validation, Supervision, Project administration, Methodology, Funding acquisition, Conceptualization. **Jorge Aguilera:** Supervision, Conceptualization. **Juan de la Casa:** Writing – review & editing, Supervision, Methodology, Conceptualization. **Luis Angel Conde:** Software, Resources, Investigation, Data curation. **Jesus Montes Romero:** Software, Resources. **Vlada Pleshcheva:** Validation, Formal analysis. **Brando Xavier Calsi:** Formal analysis, Data curation. **Miguel Angel Sevillano Bendezú:** Writing – original draft, Visualization, Software, Methodology,Formal analysis, Data curation, Conceptualization.

Declaration of Competing Interest

The authors declare the following financial interests/personal relationships which may be considered as potential competing interests: Jan Amaru Palomino Tofflinger reports financial support was provided by PROCIENCIA. Miguel Angel Sevillano Bendezu reports financial support was provided by CONCYTEC. If there are other authors, they declare that they have no known competing financial interests or personal relationships that could have appeared to influence the work reported in this paper.

Data availability

Data will be made available on request.

Acknowledgements

This work received financial support from PROCIENCIA through contract PE501078395-2022. M. A. Sevillano-Bendezú acknowledges the doctoral scholarship of CONCYTEC through PROCIENCIA, contract N°236-2015-FONDECYT and the financial support "Ayudas de la EDUJA para la realización de tesis doctorales en régimen de cotutela internacional" granted by the University of Jaen. J. A. Töfflinger acknowledges the financial support from the Academic Office of Institutional Affairs and the Vicechancellorship for Research (CAP Grupal PI0997) of the Pontificia Universidad Católica del Perú.

Appendix A

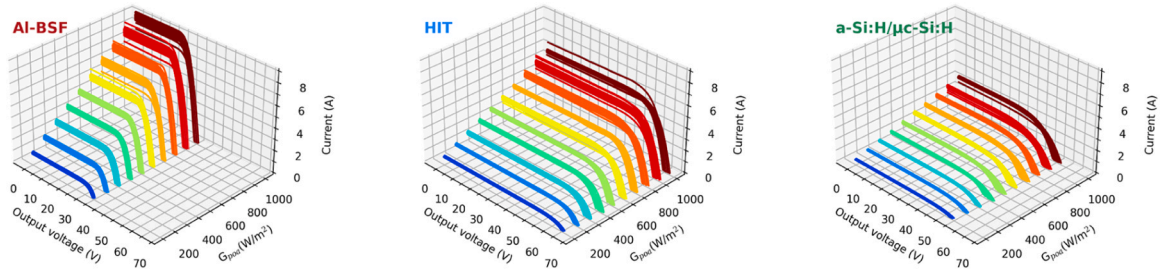

Fig. A1. Experimental *I-V* curves for each G_{poa} level and PV technology: Al-BSF, HIT, a-Si:H/µc-Si:H.

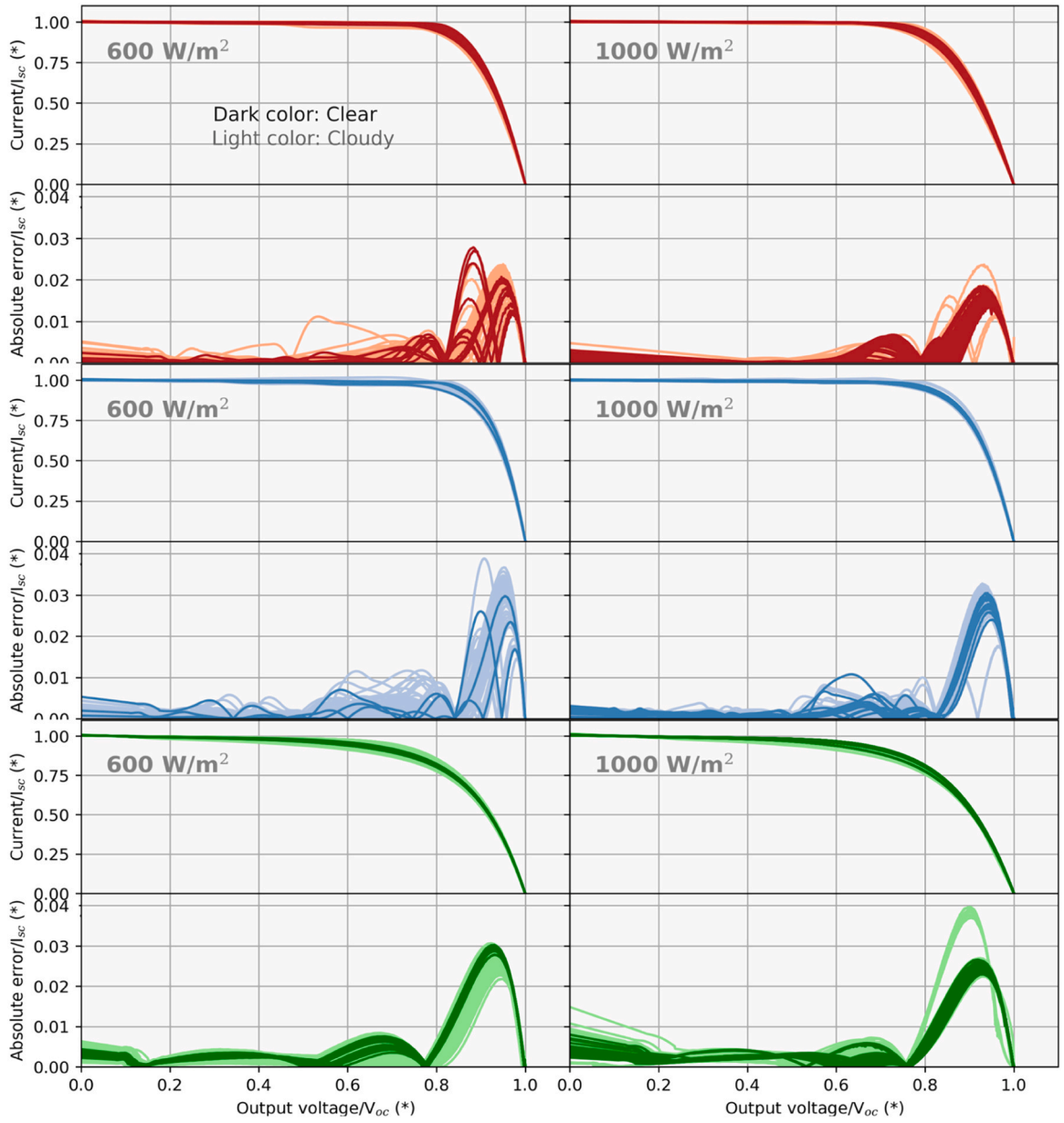

Fig. A2. Experimental *I-V* curves and absolute error normalized by the experimental short circuit current (*absolute error*/ I_{sc}) by De Blas et al. method for 600 and 1000 W/m^2 and PV module technology: Al-BSF (red), HIT (blue), a-Si:H/μc-Si:H (green).

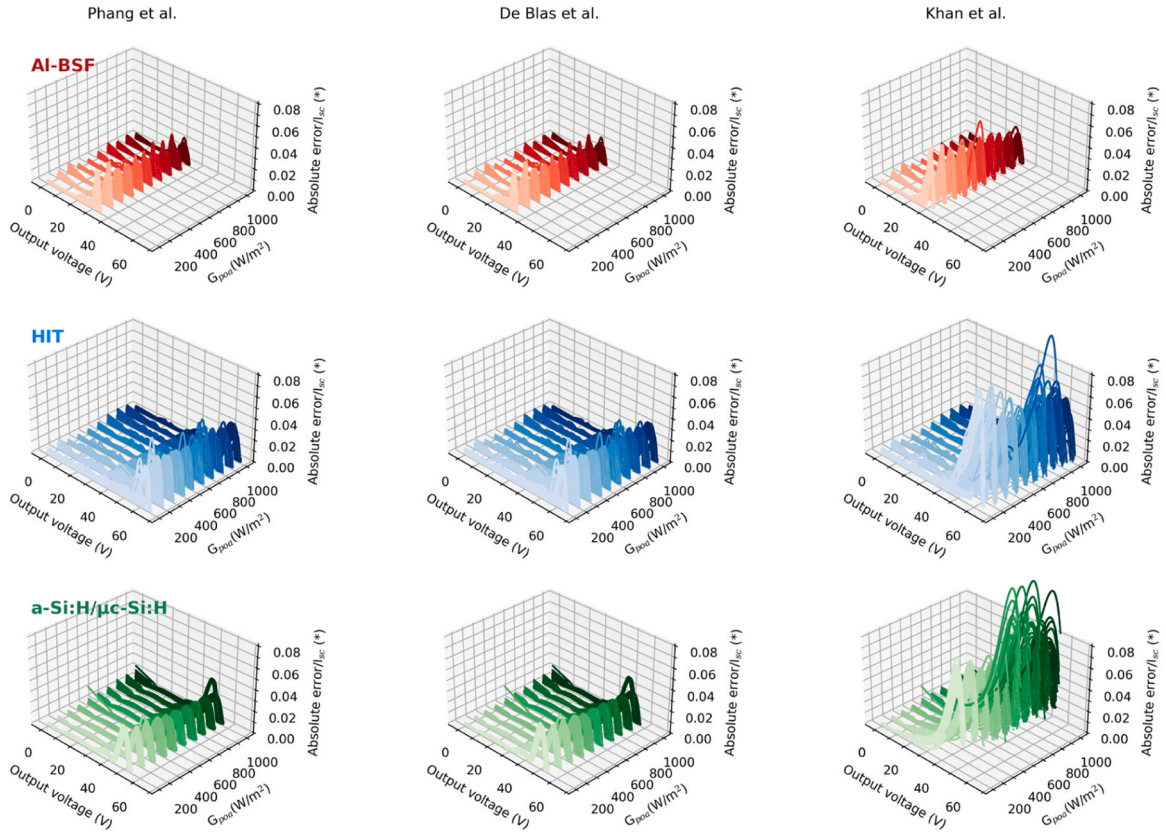

Fig. A3. Absolute error between the experimental and simulated *I-V* curves normalized by the experimental short circuit current *absolute error*/ I_{sc} along the V_{oc} for each G_{poa} level and each extraction method: In red for Al-BSF, blue for HIT, and green for a-Si:H/µc-Si:H.

References

Abbassi, R., Abbassi, A., Jemli, M., Chebbi, S., 2018. Identification of unknown parameters of solar cell models: a comprehensive overview of available approaches. Renew. Sustain. Energy Rev. 90, 453–474.

Abdulrazzaq, A.K., Bognár, G., Plesz, B., 2020. Accurate method for PV solar cells and modules parameters extraction using I–V curves *J.* King Saud. Univ. Eng. Sci. 1–11.

Al Tarabsheh, A., Akmal, M., Ghazal, M., 2017. Series connected photovoltaic cells-Modelling and analysis. Sustain 9.

Alam, D.F., Yousri, D.A., Eteiba, M.B., 2015. Flower Pollination Algorithm based solar PV parameter estimation. Energy Convers. Manag. 101, 410–422.

Ali, F., Sarwar, A., Ilahi Bakhsh, F., Ahmad, S., Ali Shah, A., Ahmed, H., 2023. Parameter extraction of photovoltaic models using atomic orbital search algorithm on a decent basis for novel accurate RMSE calculation. Energy Convers. Manag. 277, 116613.

Arabshahi, M.R., Torkaman, H., Keyhani, A., 2020. A method for hybrid extraction of single-diode model parameters of photovoltaics. Renew. Energy 158, 236–252.

Baig, M.Q., Khan, H.A., Ahsan, S.M., 2020. Evaluation of solar module equivalent models under real operating conditions - A review. J. Renew. Sustain. Energy 12.

Batzelis, E.I., Anagnostou, G., Chakraborty, C., Pal, B.C., 2020. Computation of the Lambert W function in photovoltaic modeling. In: Zamboni, G., Petrone, W. (Eds.), Lecture Notes in Electrical Engineering, ELECTRIMACS 2019, *615*. Springer, Cham, pp. 583–595.

Belghachi, A., Limam, N., 2017. Effect of the absorber layer band-gap on CIGS solar cell. Chin. J. Phys. 55, 1127–1134.

Braid, J.L., 2019. Accurate Linear I-V Extraction of Ideality. Ser. Shunt Resist. Conf. Rec. IEEE Photovolt. Spec. Conf. 368–71.

Breitenstein, O., 2014. An alternative one-diode model for illuminated solar cells. Energy Procedia 55, 30–37.

Breitenstein, O., Rakotoniaina, J.P., Al Rifai, M.H., Werner, M., 2004. Shunt types in crystalline silicon solar cells. Prog. Photovolt. Res. Appl. 12, 529–538.

Breitenstein, O., Rakotoniaina, J.P., Van Der Heide, A.S.H., Carstensen, J., 2005. Series resistance imaging in solar cells by lock-in thermography. Prog. Photovolt. Res. Appl. 13, 645–660.

Breitenstein, O., Altermatt, P., Kamspeck, K., Schenk, A., 2006. The origin of ideality factors n > 2 of shunts and surfaces in the dark I-V curves of Si 625 solar cells. Conf. Eur. Photovolt. Sol. Energy Conf. Dresd., Ger. 21.

Caballero, J.A., Fernandez, E.F., Theristis, M., Almonacid, F., Nofuentes, G., 2018. Spectral corrections based on air mass, aerosol optical depth, and precipitable water for PV performance modeling. IEEE J. Photovolt. 8, 552–558.

Cáceres, M., Firman, A., Montes-Romero, J., Mayans, A.R.G., Vera, L.H., Fernández, E.F., de la Casa Higueras, J., 2020. Low-cost I–V tracer for PV modules under real operating conditions. Energies 13 (17), 1.

Caprioglio, P., Wolff, C.M., Sandberg, O.J., Armin, A., Rech, B., Albrecht, S., Neher, D., Stolterfoht, M., 2020. On the origin of the ideality factor in perovskite solar cells. Adv. Energy Mater. 10, 2000502.

Chegaar, M., Hamzaoui, A., Namoda, A., Petit, P., Aillerie, M., Herguth, A., 2013. Effect of illumination intensity on solar cells parameters. Energy Procedia 36, 722–729.

Chin, V.J., Salam, Z., Ishaque, K., 2015. Cell modelling and model parameters estimation techniques for photovoltaic simulator application: A review. Appl. Energy 154, 500–519.

Conde, L.A., Angulo, J.R., Sevillano-Bendezú, M.Á., Nofuentes, G., Töfflinger, J.A., de la Casa, J., 2021. Spectral effects on the energy yield of various photovoltaic technologies in Lima (Peru). Energy 223, 120034.

Conde Mendoza, L.A., Carhuavilca, A., Perich, R., Montes-Romero, J., Angulo, J., Guerra, A., Muñoz, E., de la Casa, J., 2019. Performance evaluation and characterization of different photovoltaic technologies under the coastal, desertic climate conditions of Lima, Peru. In: Proceedings of the ISES Solar World Congress 2019. International Solar Energy Society, Freiburg, Germany, pp. 1–11.

Corless, R.M., Gonnet, G.H., Hare, D.E.G., Jeffrey, D.J., Knuth, D.E., 1996. On the Lambert W function. Adv. Comput. Math. 5, 329–359.

Cubas, J., Pindado, S., De Manuel, C., 2014. Explicit expressions for solar panel equivalent circuit parameters based on analytical formulation and the lambert W-function. Energies 7, 4098–4115.

De Blas, M.A., Torres, J.L., Prieto, E., García, A., 2002. Selecting a suitable model for characterizing photovoltaic devices. Renew. Energy 25, 371–380.

De Soto, W., Klein, S.A., Beckman, W.A., 2006. Improvement and validation of a model for photovoltaic array performance. Sol. Energy 80, 78–88.

Deutsche Gesellschaft für, 2013. Sonnenenergie. Planning and Installing Photovoltaic Systems. A Guide for Installers, Architects and Engineers. third ed. Gosport. Routledge.

Dupré, O., Vaillon, R., Green, M.A., 2015. Physics of the temperature coefficients of solar cells. Sol. Energy Mater. Sol. Cells 140, 92–100.

El-Naggar, K.M., AlRashidi, M.R., AlHajri, M.F., Al-Othman, A.K., 2012. Simulated Annealing algorithm for photovoltaic parameters identification. Sol. Energy 86, 266–274.

Enfield, D.B., 1981. Thermally driven wind variability in the planetary boundary layer above Lima, Peru. J. Geophys. Res. 86, 2005–2016.

F. Holmgren, W., W. Hansen, C., A. Mikofski, M., 2018. Pvlib Python: a Python package for modeling solar energy systems. J. Open Source Softw. 3, 884.

Fahim, S.R., Hasanien, H.M., Turky, R.A., Aleem, S.H.E.A., Ćalasan, M., 2022. A comprehensive review of photovoltaic modules models and algorithms used in parameter extraction. Energies 15, 1–56.
Farias-Basulto, G.A., Ulbrich, C., Schlatmann, R., Klenk, R., 2023. Periodical evaluation of photovoltaic modules and diode parameter extraction method using multiple linear regression models. Jpn. J. Appl. Phys. 62, SK1023.
Fernández, E.F., Siefer, G., Almonacid, F., Loureiro, A.J.G., Pérez-Higueras, P., 2013. A two subcell equivalent solar cell model for III-V triple junction solar cells under spectrum and temperature variations. Sol. Energy 92, 221–229.
Fernández, E.F., Montes-Romero, J., de la Casa, J., Rodrigo, P., Almonacid, F., 2016. Comparative study of methods for the extraction of concentrator photovoltaic module parameters. Sol. Energy 137, 413–423.
Frühauf, F., Breitenstein, O., 2017. DLIT- versus ILIT-based efficiency imaging of solar cells. Sol. Energy Mater. Sol. Cells 169, 195–202.
Garoudja, E., Kara, K., Chouder, A., Silvestre, S., 2015. Parameters extraction of photovoltaic module for long-term prediction using artifical bee colony optimization. In: 3rd International Conference on Control, Engineering & Information Technology (CEIT), *2015*. IEEE, pp. 1–6.
Ghani, F., Rosengarten, G., Duke, M., Carson, J.K., 2014. The numerical calculation of single-diode solar-cell modelling parameters. Renew. Energy 72, 105–112.
Gu, Z., Xiong, G., Fu, X., Mohamed, A.W., Al-Betar, M.A., Chen, H., Chen, J., 2023. Extracting accurate parameters of photovoltaic cell models via elite learning adaptive differential evolution. Energy Convers. Manag. 285, 116994.
Gueymard, C.A., 2008. REST2: High-performance solar radiation model for cloudless-sky irradiance, illuminance, and photosynthetically active radiation - Validation with a benchmark dataset. Sol. Energy 82, 272–285.
Hali A. and Khlifi Y. 2022 A New Method for Photovoltaic Parameters Extraction Under Variable Weather Conditions pp 565–574.
Haschke, J., Seif, J.P., Riesen, Y., Tomasi, A., Cattin, J., Tous, L., Choulat, P., Aleman, M., Cornagliotti, E., Uruena, A., Russell, R., Duerinckx, F., Champliaud, J., Levrat, J., Abdallah, A.A., Aïssa, B., Tabet, N., Wyrsch, N., Despeisse, M., Szlufcik, J., De Wolf, S., Ballif, C., 2017. The impact of silicon solar cell architecture and cell interconnection on energy yield in hot & sunny climates. Energy Environ. Sci. 10, 1196–1206.
Humada, A.M., Darweesh, S.Y., Mohammed, K.G., Kamil, M., Mohammed, S.F., Kasim, N. K., Tahseen, T.A., Awad, O.I., Mekhilef, S., 2020. Modeling of PV system and parameter extraction based on experimental data: Review and investigation. Sol. Energy 199, 742–760.
Iacono, R., Boyd, J.P., 2017. New approximations to the principal real-valued branch of the Lambert W-function. Adv. Comput. Math. 43, 1403–1436.
Jardine, C., Betts, T., Gottschlg, R., Infield, D.G., Lane, K., 2002. Influence of spectral effects on the performance of multijunction amorphous silicon cells. *Proc. PV Eur. – PV Technol. Energy Solut.* (Rome, Italy).
Karmalkar, S., Haneefa, S., 2008. A physically based explicit J – V model of a solar cell for simple design calculations. IEEE Electron Device Lett. 29, 449–451.
Khan, F., Baek, S.H., Park, Y., Kim, J.H., 2013. Extraction of diode parameters of silicon solar cells under high illumination conditions. Energy Convers. Manag. 76, 421–429.
Khan, F., Al-Ahmed, A., Al-Sulaiman, F.A., 2021. Critical analysis of the limitations and validity of the assumptions with the analytical methods commonly used to determine the photovoltaic cell parameters. Renew. Sustain. Energy Rev. 140, 110753.
Khanna, V., Das, B.K., Bisht, D., Vandana, Singh, P.K., 2015. A three diode model for industrial solar cells and estimation of solar cell parameters using PSO algorithm. Renew. Energy 78, 105–113.
Kharchouf, Y., Herbazi, R., Chahboun, A., 2022. Parameter's extraction of solar photovoltaic models using an improved differential evolution algorithm. Energy Convers. Manag. 251, 114972.
Li, S., Gu, Q., Gong, W., Ning, B., 2020. An enhanced adaptive differential evolution algorithm for parameter extraction of photovoltaic models. Energy Convers. Manag. 205, 112443.
Ma, X., Huang, W.H., Schnabel, E., Kohl, M., Brynjarsdottir, J., Braid, J.L., French, R.H., 2019. Data-Driven I-V Feature Extraction for Photovoltaic Modules. IEEE J. Photovolt. 9, 1405–1412.
Mcintosh, K.R., Altermatt, P.P., Heiser, G., 2000. Depletion-region recombination in silicon solar cells: when does mDR = 2 ? *oc.16*. th EC Sol. Energy Conf. Glas. UK 0, 251–254.
Meillaud, F., Feltrin, A., Dominé, D., Buehlmann, P., Python, M., Bugnon, G., Billet, A., Parascandolo, G., Bailat, J., Fay, S., Wyrsch, N., Ballif, C., Shah, A., 2009. Limiting factors in the fabrication of microcrystalline silicon solar cells and microcrystalline/amorphous ('micromorph') tandems. Philos. Mag. 89, 2599–2621.
Merten, J., Asensi, J.M., Voz, C., Shah, A.V., Platz, R., Andreu, J., 1998. Improved equivalent circuit and analytical model for amorphous silicon solar cells and modules. IEEE Trans. Electron Devices 45, 423–429.
Mialhe, P., Charles, J.P., Khoury, A., Bordure, G., 1986. The diode quality factor of solar cells under illumination. J. Phys. D. Appl. Phys. 19, 483–492.
Mlazi, N.J., Mayengo, M., Lyakurwa, G., Kichonge, B., 2024. Mathematical modeling and extraction of parameters of solar photovoltaic module based on modified Newton–Raphson method. Results Phys. 57.
Montes-Romero, J., Piliougine, M., Muñoz, J.V., Fernández, E.F., De La Casa, J., 2017. Photovoltaic device performance evaluation using an open-hardware system and standard calibrated laboratory instruments. Energies 10.
Montes-Romero, J., Almonacid, F., Theristis, M., de la Casa, J., Georghiou, G.E., Fernández, E.F., 2018. Comparative analysis of parameter extraction techniques for the electrical characterization of multi-junction CPV and m-Si technologies. Sol. Energy 160, 275–288.
Nofuentes, G., Almonacid, G., 1998. An approach to the selection of the inverter for architecturally integrated photovoltaic grid-connected systems. Renew. Energy 15, 487–490.
Nofuentes, G., de la Casa, J., Torres-Ramírez, M., Alonso-Abella, M., 2013. Solar spectral and module temperature influence on the outdoor performance of thin film PV modules deployed on a sunny inland site. Int. J. Photoenergy 2013, 1–12.
Nouri, L., Ihfa, F.Z., Oubella, Y.A., Sakhi, Z., Bennai, M., 2024. Single-diode multi-junction solar cell models five-parameter estimation method. Indian J. Phys. 98, 629–637.
Oulcaid, M., El Fadil, H., Ammeh, L., Yahya, A., Giri, F., 2020. Parameter extraction of photovoltaic cell and module: Analysis and discussion of various combinations and test cases. Sustain. Energy Technol. Assess. 40, 100736.
Padovani, F.A., Stratton, R., 1966. Field and thermionic-field emission in Schottky barriers. Solid State Electron 9, 695–707.
Phang, J.C.H., Chan, D.S.H., Phillips, J.R., 1984. Accurate analytical method for the extraction of solar cell model parameters. Electron. Lett. 20, 406–408.
Phillips, A.B., Subedi, K.K., Liyanage, G.K., Alfadhili, F.K., Ellingson, R.J., Heben, M.J., 2020. Understanding and Advancing Bifacial Thin Film Solar Cells. ACS Appl. Energy Mater. 3, 6072–6078.
Polo, J., Wilbert, S., Ruiz-Arias, J.A., Meyer, R., Gueymard, C., Súri, M., Martín, L., Mieslinger, T., Blanc, P., Grant, I., Boland, J., Ineichen, P., Remund, J., Escobar, R., Troccoli, A., Sengupta, M., Nielsen, K.P., Renne, D., Geuder, N., Cebecauer, T., 2016. Preliminary survey on site-adaptation techniques for satellite-derived and reanalysis solar radiation datasets. Sol. Energy 132, 25–37.
Premkumar, M., Kumar, C., Sowmya, R., 2020. Mathematical modelling of solar photovoltaic cell/panel/array based on the physical parameters from the manufacturer's datasheet. Int. J. Renew. Energy Dev. 9, 7–22.
Ramesh, S., Tuomiranta, A., Hajjiah, A., Meuris, M., Vermang, B., Poortmans, J., 2022. Physics-based electrical modelling of CIGS thin-film photovoltaic modules for system-level energy yield simulations. npj Flex. Electron. 6, 1–9.
Rau, U., Jasenek, A., Schock, H.W., Engelhardt, F., Meyer, T., 2000. Electronic loss mechanisms in chalcopyrite based heterojunction solar cells. Thin Solid Films 361, 298–302.
Reno, M.J., Hansen, C.W., 2016. Identification of periods of clear sky irradiance in time series of GHI measurements. Renew. Energy 90, 520–531.
Riben, A.R., Feucht, D.L., 1966. Electrical Transport in nGe-pGaAs Heterojunctions. Int. J. Electron. 20, 583–599.
Ruschel, C.S., Gasparin, F.P., Krenzinger, A., 2021. Experimental analysis of the single diode model parameters dependence on irradiance and temperature. Sol. Energy 217, 134–144.
Sah, C., Noyce, R.N., Shockley, W., 1956. Junctions and P-N Junction Characteristics. Proc. IRE 1, 1228–1243.
Sandberg, O.J., Armin, A., 2019. On the effect of surface recombination in thin film solar cells, light emitting diodes and photodetectors. Synth. Met. 254, 114–121.
Schroder, D.K., 2005. Semicond. Mater. Device Charact.: Third Ed.
Schweiger, M., Herrmann, W., Gerber, A., Rau, U., 2017. Understanding the energy yield of photovoltaic modules in different climates by linear performance loss analysis of the module performance ratio. IET Renew. Power Gener. 11, 558–565.
Sengupta, M., Xie, Y., Lopez, A., Habte, A., Maclaurin, G., Shelby, J., 2018. The National Solar Radiation Data Base (NSRDB). Renew. Sustain. Energy Rev. 89, 51–60.
Sevillano-Bendezú, M.A., Conde, L.A., De La Casa, J., Töfflinger, J.A., 2022. Average photon energy assessment based on modelled spectra from the National Solar Radiation Database for Lima, Peru. J. Phys. Conf. Ser. 2180, 0–6.
Sevillano-Bendezú, M.A., Khenkin, M., Nofuentes, G., de la Casa, J., Ulbrich, C., Töfflinger, J.A., 2023. Predictability and interrelations of spectral indicators for PV performance in multiple latitudes and climates. Sol. Energy 259, 174–187.
Shen, L., Li, Z., Ma, T., 2020. Analysis of the power loss and quantification of the energy distribution in PV module. Appl. Energy 260, 114333.
Shockley, W., 1953. Electrons and Holes in Semiconductors.
Solís-Alemán, E.M., de la Casa, J., Romero-Fiances, I., Silva, J.P., Nofuentes, G., 2019. A study on the degradation rates and the linearity of the performance decline of various thin film PV technologies. Sol. Energy 188, 813–824.
Stein J.S., Mccaslin S., Hansen C.W., Boyson W.E. and Robinson C.D. 2014 Measuring PV System Series Resistance Without Full IV Curves 2032–2036.
Steingrube, S., Breitenstein, O., Ramspeck, K., Glunz, S., Schenk, A., Altermatt, P.P., 2011. Explanation of commonly observed shunt currents in c-Si solar cells by means of recombination statistics beyond the Shockley-Read-Hall approximation. J. Appl. Phys. 110.
Sturiale, A., Li, H.T., Rath, J.K., Schropp, R.E.I., Rubinelli, F.A., 2009. Exploring dark current voltage characteristics of micromorph silicon tandem cells with computer simulations. J. Appl. Phys. 106.
Taciuc, M., Crăciunescu, A., 2017. Application of the Lambert W-function for a PV module parameters' estimation. AIP Conf. Proc. 1863.
Tian, H., Mancilla-David, F., Ellis, K., Muljadi, E., Jenkins, P., 2012. A cell-to-module-to-array detailed model for photovoltaic panels. Sol. Energy 86, 2695–2706.
Ulbrich, C., Jordan, D.C., Kurtz, S.R., Gerber, A., Rau, U., 2015. Direct analysis of the current density vs. voltage curves of a CdTe module during outdoor exposure. Sol. Energy 113, 88–100.
Williams, S.R., Betts, T.R., Helf, T., Gottschalg, R., Beyer, H.G., Infield, D.G., 2003. Modelling long-term module performance based on realistic reporting conditions with consideration to spectral effects Third World Conference on Photovoltaic Energy Conversion, 2003. Proceedings vol 2, 1908–1911. Vol.2.
Yang, B., Wang, J., Zhang, X., Yu, T., Yao, W., Shu, H., Zeng, F., Sun, L., 2020. Comprehensive overview of meta-heuristic algorithm applications on PV cell parameter identification. Energy Convers. Manag. 208, 112595.

Ye, M., Wang, X., Xu, Y., 2009. Parameter extraction of solar cells using particle swarm optimization. J. Appl. Phys. 105, 094502.
Yoon, J.H., Park, J.K., Kim, W.M., Lee, J., Pak, H., Jeong, J.H., 2015. Characterization of efficiency-limiting resistance losses in monolithically integrated Cu(In,Ga)Se 2 solar modules. Sci. Rep. 5, 1–9.
Yousuf, H., Zahid, M.A., Khokhar, M.Q., Park, J., Ju, M., Lim, D., Kim, Y., Cho, E.C., Yi, J., 2022. Cell-to-module simulation analysis for optimizing the efficiency and power of the photovoltaic module. Energies 15.
Zamalloa-Jara, M.A., Sevillano-Bendezú, M.Á., Ulbrich, C., Nofuentes, G., Grieseler, R., Töfflinger, J.A., 2023. Overirradiance conditions and their impact on the spectral distribution at low- and mid-latitude sites. Sol. Energy 259, 99–106.
Zhang, Y., 2021. Neural Network Algorithm With Reinforcement Learning for Parameters Extraction of Photovoltaic Models. IEEE Trans. Neural Netw. Learn. Syst. 1, 11.
Zhu D., Xu J., Noemaun A.N., Kim J.K., Schubert E.F., Crawford M.H. and Koleske D.D. 2009 The Origin of the High Diode-ideality Factors in GaInN/GaN Multiple Quantum Well Light-emitting Diodes 2–4.